CMS Physics Analysis Summary

Contact: cms-phys-conveners-ftr@cern.ch 2018/12/21

Prospects for HH measurements at the HL-LHC

The CMS Collaboration

Abstract

The prospects for the study of Higgs boson pair production at the High-Luminosity LHC with the CMS detector are presented. Five decay channels, bbbb, bbWW, bb$\tau\tau$, bb$\gamma\gamma$, and bbZZ, are studied. Analyses are developed using a parametric simulation of the upgraded detector response and optimised for a projected integrated luminosity of 3000 fb^{-1}. The statistical combination of the five decay channels results in an expected significance for the standard model HH signal of 2.6σ. Projections are also presented for the measurement of the Higgs boson self-coupling λ_{HHH}. The expected 68 and 95% confidence level intervals for the coupling modifier $\kappa_\lambda = \lambda_{\mathrm{HHH}}/\lambda_{\mathrm{HHH}}^{\mathrm{SM}}$ are $[0.35, 1.9]$ and $[-0.18, 3.6]$, respectively.

Contents

1 Introduction

The discovery of a scalar boson with a mass of about 125 GeV by the ATLAS and CMS Collaborations [1–3], and the determination of its properties so far consistent with those expected for the Higgs boson (H) of the standard model of particle physics (SM) [4], has stimulated interest for a detailed exploration and understanding of the Brout–Englert–Higgs (BEH) mechanism [5–7]. The SM predicts the existence of Higgs boson self-interactions, whose properties are directly determined by the structure of the BEH scalar potential. The study of the production of Higgs boson pairs (HH) represents therefore a crucial test of the SM since it gives experimental access to the Higgs boson self-coupling (λ_{HHH}) and thus to the structure of the BEH potential itself. Moreover, HH production represents a unique way to probe the existence of physics beyond the standard model (BSM) that may manifest as a modification of λ_{HHH}. In general, low energy scale effects of some high energy scale physics, as described in the context of an effective theory (EFT) [8], can result as contact interaction terms in the Lagrangian. Terms which can affect the double Higgs production are contact interactions between the HH pair and gluons (ggHH) and top quarks (ttHH), as well as a contact interaction between one Higgs boson and two gluons that we expect to be constrained in single Higgs boson measurements. The presence of these additional contributions will result in an anomalous HH production cross section and modified kinematic properties of the HH system.

In the SM, the dominant HH production mechanism in pp collisions is via gluon fusion, with an expected cross section of $31.05^{+2.2\%}_{-5.0\%}$ fb at $\sqrt{s} = 13$ TeV and $36.69^{+2.1\%}_{-4.9\%}$ at 14 TeV. These values were computed at the next-to-next-to-leading order (NNLO) of the perturbative quantum chromodynamics (QCD) calculation, including next-to-next-to-leading-logarithm (NNLL) corrections and finite top quark mass effects [9]. Because of the smallness of the cross section and the presence of backgrounds, searches for HH productions based on the current Run II dataset are not yet sensitive to SM HH production; large integrated luminosities are required for the experimental study of this very rare process.

The High-Luminosity LHC (HL-LHC) will provide a unique opportunity to study HH production as predicted in the SM and identify possible deviations induced by BSM physics in the signal cross section or properties. Upgrades of the LHC machine will increase the peak instantaneous luminosity to $5 - 7.5 \times 10^{34}\,\mathrm{cm}^{-2}\,\mathrm{s}^{-1}$ and the CMS experiment will collect more than 3000 fb^{-1} over a decade of operation. The high instantaneous luminosity will lead to 140 to 200 additional interactions per bunch crossing. This pileup will constitute a formidable challenge for the experiment both in terms of event reconstruction and radiation damage. A comprehensive detector upgrade program is under development to maintain and improve the detector performance under these challenging conditions.

The projected sensitivity to HH at the HL-LHC has so far been studied by the ATLAS [10–13] and CMS [14, 15] Collaborations either using a parametric simulation of the detector performance or with an extrapolation of the Run II analysis results. In both cases, the projected combined sensitivity to HH production is at the level of about 2σ or below. It is important to remark here that the usage of a parametric simulation requires a comprehensive knowledge of the expected upgraded detector performance. Very recent developments in the detector performance from CMS upgrade studies are not accounted in the referenced results. Similarly, the extrapolation of the current results cannot account for the optimisation of the analysis strategy to the large dataset collected at the HL-LHC.

Updated projections of the sensitivity have recently been developed by the CMS Collaboration to study the impact of the subsystem upgrades on the physics program, as described in the Technical Design Report (TDR) of the inner tracker [16], the barrel electromagnetic [17] and the

endcap high-granularity [18] calorimeters.

The work described in this document improves and extends the previous projections to provide an updated and comprehensive study of the prospects for HH measurements at the HL-LHC. A parametric simulation, as detailed in Section 3, is used to model the upgraded detector response and simulate its performance considering the experience and understanding achieved in the preparation of the aforementioned TDRs. The five decay channels bbbb, bb$\tau\tau$, bbWW (WW $\to \ell\nu\ell'\nu'$ with $\ell, \ell' = \mathrm{e}, \mu$), bb$\gamma\gamma$, and bbZZ (ZZ $\to \ell\ell\ell'\ell'$ with $\ell, \ell' = \mathrm{e}, \mu$) are studied and dedicated analysis strategies are developed to exploit the HL-HLC dataset. The first four channels correspond to those expected to be the most sensitive to HH production at the HL-LHC based on the experience from Run II searches, while the very rare but clean bbZZ($\ell\ell\ell\ell$) final state is studied here for the first time. The corresponding branching fractions, computed considering a mass of the Higgs boson of 125 GeV [19], are summarised in Table 1. The event selection and analysis strategy of each channel are separately described in the following, and the sensitivity resulting from their statistical combination is discussed in Section 9.

Table 1: Branching fraction of the five decay channels considered in this document. The symbol ℓ denotes either a muon or an electron. In the bbWW decay channel, ℓ from the intermediate production of a τ lepton are also considered in the branching fraction.

Channel	$\mathcal{B}$ [%]
bbbb	33.6
bb$\tau\tau$	7.3
bbWW($\ell\nu\ell\nu$)	1.7
bb$\gamma\gamma$	0.26
bbZZ($\ell\ell\ell\ell$)	0.015

2 The CMS upgraded detector

The improvement of the performance of the CMS detector under HL-LHC conditions requires both increased radiation hardness to withstand over a decade of HL-LHC operations under high pileup and luminosity conditions, increased granularity to reduce particle occupancy and improve the object reconstruction, and increased bandwidth to accommodate higher data rates.

Both the hardware and software stages of the CMS trigger system, respectively denoted as the Level-1 (L1) and High Level Trigger (HLT), and the data acquisition system (DAQ) will undergo a substantial upgrade. The L1 trigger hardware will be replaced, allowing for an increase of its rate and latency to about 750 kHz and 12.5 μs respectively, while the HLT rate will be increased to 7.5 kHz. These values are to compare to the throughput of the current L1 and HLT systems of about 100 and 1 kHz respectively, and to a current L1 system latency of 3.8 μs. The L1 will also feature inputs from the silicon tracker, allowing real-time track fitting and particle-flow reconstruction of objects at the trigger level. The pixel and strip tracker detectors will be replaced to increase the granularity, reduce the material budget and extend the geometrical coverage. The front-end electronics of the barrel electromagnetic calorimeter (ECAL) will be upgraded to access the single-crystal information at the L1 trigger, as well as the electronics of the cathode strip chambers (CSC), resistive plate chambers (RPC) and drift tubes (DT) for muon detection. New muon detectors based on RPC and gas electron multiplier (GEM) technologies will also be installed to add redundancy, increase the geometrical coverage, and improve the trigger and reconstruction of muons in the forward region. The endcap electromagnetic and

hadron calorimeters will be replaced with a new high-granularity sampling detector (HGCal) based on silicon pad sensor and will provide highly-segmented spatial information as well as timing information for a four-dimensional reconstruction of the interaction shower shapes. Finally, the addition of a new timing detector for minimum ionizing particles (MTD) is envisaged to provide additional capabilities, beyond spatial tracking algorithms, to correctly associate the reconstructed charged particles to the production vertex and thus suppress pileup effects.

A detailed overview of the upgrade program and of the CMS detector upgrades are presented in the Technical Proposal for the Phase-II upgrade [20]. The performance in object reconstruction is detailed and summarised in Ref. [21].

3 Signal and background modelling

3.1 Simulated physics processes

The signal and background processes in pp collisions at $\sqrt{s} = 14\,\text{TeV}$ are modelled using Monte Carlo (MC) event generators, that simulate the hard process, as well as the hadronisation and fragmentation effects. They are interfaced with the DELPHES [22] software to model the response of the upgraded CMS detector.

The HH signal is simulated using MADGRAPH5_aMC@NLO [23] at leading order (LO) accuracy. Five different samples of SM HH production are generated for the five final states considered here. The Higgs boson branching fractions prediction in the SM is used for the normalisation of the samples, resulting in the values previously reported in Table 1. Signals corresponding to anomalous values of the λ_{HHH} coupling are modelled by weighting the SM samples as a function of the invariant mass of the HH pair and of the angle of one of the two Higgs bosons with respect to the beam line in the reference of the HH system, following the procedure detailed in Ref. [24]. The same technique is also used to model the so-called shape benchmark signals, i.e. signals corresponding to specific combinations of Higgs boson effective couplings which kinematic properties may be used to approximately represent broader regions of the EFT parameter space. The definition of the shape benchmarks is given in [25].

Several background sources are considered for each decay channel, as detailed in the corresponding section of this documents.

Top quark processes are simulated using POWHEG [26–29] and multiparton interactions, parton shower, and hadronization effects are simulated with PYTHIA 8 [30]. The $\text{t}\bar{\text{t}}$ production is normalised to the theoretical production cross section at $\sqrt{s} = 14\,\text{TeV}$ computed at NNLO+NNLL of $984.50^{+23.21}_{-34.69}(\text{scale})^{+41.31}_{-41.31}(\text{PDF} + \alpha_{\text{S}})^{+27.14}_{-26.29}(\text{mass})$ [31]. Single top quark production in the tW channel is normalised to the theoretical prediction at NNLO precision of $84.4 \pm 2.0(\text{scale})^{+3.00}_{-4.80}(\text{PDF})$ [32, 33]. The production of top quark pairs in association with Z bosons pairs is simulated with MADGRAPH5_aMC@NLO forcing the four lepton decay of the ZZ system.

Drell-Yan production of leptons pairs $\text{Z}/\gamma^* \to \ell\ell$ and of $\text{W} \to \ell\nu$ in association with jets are simulated at the LO precision using MADGRAPH5_aMC@NLO and normalised to the generator cross section at the same precision order. To increase the number of Z/γ^* events that satisfy the event selections, inclusive samples are complemented by simulations in selected regions of the scalar sum of the transverse momentum of the partons emitted at matrix element level and of the invariant mass of the $\ell\ell$ system.

Multijet production from QCD interactions is simulated using MADGRAPH5_aMC@NLO at LO

accuracy. To increase the selection efficiency for the projection in the bbbb final state, the presence of at least one b quark emitted at matrix level is also required. Samples are generated in exclusive intervals of the scalar sum of the transverse momentum of the partons emitted at matrix element level and combined using the relative cross section. An inclusive sample, where generated events are required to contain a pair of partons with invariant mass larger than 1 TeV, is also used to improve the description for the phase space of highly boosted jets. The overall normalisation for the multijet background is obtained from a comparison between Run II data and MC produced with the same generator at $\sqrt{s} = 13$ TeV.

Single Higgs boson production in gluon ($gg \rightarrow H$) and vector boson (VBF) fusion, and in associated production with top quarks ($t\bar{t}H$) and vector bosons (VH), is considered as a background for HH production. Decays of the Higgs boson are forced to exclusive final states to increase the acceptance for the HH decay channels studies, and different generators are used. For all the aforementioned processes where the Higgs boson decays to $ZZ^* \rightarrow \ell\ell\ell\ell$, the MADGRAPH5_aMC@NLO generator is used. For the decays of the Higgs boson to photon pairs, MADGRAPH5_aMC@NLO is used for the $gg \rightarrow H$, VBF and VH processes, while POWHEG is used for $t\bar{t}H$. For the other channels, single Higgs samples for all the production modes are generated with POWHEG. Generated samples are normalised to the expected SM cross section as recommended in [19]. The $gg \rightarrow H$ production cross section is computed at the next-to-next-to-next-to-leading order (N^3LO) in perturbative QCD and at NLO in electroweak (EW) corrections. The VBF and WH processes cross sections are computed at NNLO QCD and NLO EW accuracies, and the $t\bar{t}H$ cross section is computed at NLO QCD and NLO EW accuracies. Finally, the ZH cross section is computed at NNLO QCD and NLO EW accuracy for quark-initiated contributions and at NLO QCD accuracy with NLL effects for the gluon fusion-induced component.

3.2 CMS detector response and object reconstruction

Both the signal and background samples are processed with the DELPHES fast parametric simulation software to simulate the response of the upgraded CMS detector and account for the pileup contributions by overlaying an average of 200 minimum bias interaction events simulated with PYTHIA 8. The DELPHES software simulates the performance of reconstruction and identification algorithms for electrons, muons, tau decays to hadrons (τ_h) and a neutrino, photons, jets including those containing heavy flavour particles, and the missing transverse momentum vector $\vec{p}_T^{\,miss}$, defined as the projection onto the plane perpendicular to the beam axis of the negative vector sum of the momenta of all reconstructed particle-flow objects in an event. The resolution, energy and momentum scale, efficiencies, and misidentification rates for the various objects have been extensively compared and tuned to reproduce the performance obtained with a full simulation of the CMS detector based on GEANT4 [34] and the use of reconstruction algorithms tuned to the HL-LHC environment. In those cases where the reconstruction algorithms have not yet been developed or finalised, the parametrisation follows assumptions based on the Run II object performance and on the studies prepared for the CMS detector Technical Design Reports.

The simulation of the electron reconstruction is initiated by generator-level electrons, with a detection efficiency that parametrised in energy and pseudorapidity. The energy resolution of reconstructed electrons is a function of the ECAL and tracker resolutions. Similarly, the simulation of muon reconstruction is seeded by generator-level muons, applying a parametric reconstruction and identifications efficiency. The momentum of reconstructed muons is obtained via Gaussian smearing of the generator-level muon 4-momenta, with a resolution parametrised by transverse momentum and pseudorapidity.

Photons are reconstructed from neutral energy excess in a simplified version of the electromagnetic calorimeter. The efficiency for photons and jet backgrounds are parametrised based on studies of the upgraded CMS detector and correspond to the performance of a multivariate identification algorithm combined with an isolation selection.

Hadronic jets are reconstructed with a particle-flow algorithm run on simulated tracks and on the energy deposits in the ECAL, HCAL, and HGCal. The particle-flow candidates are clustered via sequential recombination of tracks and calorimeter deposits using the anti-k_T algorithm [35, 36] operated with a distance parameters R of 0.4. Pileup mitigation is performed using the "PileUp Per Particle Identification" (PUPPI) algorithm [37].

The missing transverse momentum $\vec{p}_T^{\,miss}$ is calculated for each event using particle-flow (PF) objects and corrected using PUPPI.

The efficiency of b jet identification and the corresponding misidentification rates for light flavour quarks and gluons jets are parametrised as functions of the jet p_T and η, depending on the underlying jet flavour as determined by a geometric match with generated partons. The parametrised b tagging performance considers the improvements following the inclusion of the MTD detector measurements [38].

The efficiency of τ_h identification and hadron jet misidentification rates are parametrised as functions of the jet p_T and η. Reconstructed jets are geometrically matched with τ_h objects at generator level to determine whether a jet candidate is a genuine τ_h or a quark or gluon jet. Parametrised probabilities corresponding to efficiency and misidentification rates, obtained from studies based on full CMS simulation, are consequently applied.

We do note that the aforementioned improvements in the b tag efficiency following the inclusion of the MTD detector information only correspond to the removal of spurious tracks in the reconstructed jets, effectively acting as suppression of the pileup effects, but that the track timing information is not used directly in a dedicated training of a b tag discriminant. Moreover, further improvements following the inclusion of the MTD detector are expected in the lepton, τ_h and photon isolation performance, as well as in the rejection of additional jets erroneously associated to the main production vertex. Improvements in the results described in this work may consequently be expected from a full, optimal use of the timing information.

3.3 Systematic uncertainties

Systematic uncertainties in the modelling of the signal and background processes due to theoretical (normalisation cross sections) and experimental effects (object reconstruction performance and background estimation) are considered. The assumption for the values reported below are discussed in detail in Ref. [21].

An uncertainty on the total integrated luminosity of 1% is considered. It is correlated in all the channels across all the processes that are assumed to be modelled with a MC simulation at the HL-LHC.

Uncertainties on the b tag efficiency are parametrised as a function of the jet η and p_T, and amount to about 1% for genuine b jets with $p_T < 300\,\text{GeV}$ and range between 2 and 6% for larger p_T values. An uncertainty of 1% is also assumed for the b tag efficiency of subjets identified within large-radius jets. The uncertainty on the scale of the reconstructed jets ranges between 0.2 and 2% depending on the source considered and is applied by varying the jet p_T by the corresponding value and checking the changes in the processes yields.

Uncertainties in the electron identification and isolation efficiencies amount to 2.5% and 0.5%

for p_T below and above 20 GeV, respectively. The muon identification and isolation efficiency uncertainty corresponds to 0.5% for all the p_T values considered. For τ_h objects, this uncertainty amounts to 5% as in the Run II analyses. The uncertainties in the photon reconstruction and identification efficiency correspond to 1%, while their energy scale and resolution are assumed to be determined with an accuracy of 0.5 ad 5%, respectively.

Specific uncertainties in the modelling of the main physics processes are also considered and discussed in the context of the relevant analyses. Triggers are assumed to be fully efficient in the phase space considered, and the corresponding uncertainties are included in the object reconstruction and identification uncertainties.

The uncertainties in the theoretical cross sections used for the normalisation of simulated processes are assumed to be reduced by a factor of 1/2 with respect to the current value.

4 HH → bbbb

While characterised by the largest branching fraction among the HH final states, the bbbb decay channel suffers from a large contamination from the multijet background that makes it experimentally challenging. Two complementary strategies are explored here to identify the signal contribution. For those events where the four jets from the HH → bbbb decay can all be reconstructed separately, also referred to as the "resolved" topology, the use of multivariate methods is explored to efficiently identify the signal contribution in the overwhelming background. In cases where the invariant mass of the HH system, m_{HH}, is large, the high Lorentz boost of both Higgs bosons may results in a so-called "boosted" event topology where the two jets from a H → $b\bar{b}$ decay overlap and are reconstructed as a single, large-area jet. Resolved topologies correspond to the large majority of SM HH events, giving the largest sensitivity on this signal. Boosted topologies help to suppress the multijet background and provide sensitivity to BSM scenarios where the differential HH production cross section is enhanced at high m_{HH} by the presence of ggHH and ttHH effective contact interactions.

4.1 Event selection for resolved topologies

This work assumes the trigger efficiency to be 100% for the reconstructed object selections detailed below. This assumption is based on experience in the Run II analysis and is considered to be realistic considered the planned upgrades of the CMS trigger system, both at L1 and HLT, that will allow for an improvement and harmonisation of online and offline b tagging algorithms.

Events are preselected by requiring four jets with $p_T > 45$ GeV and $|\eta| < 3.5$ that satisfy the medium b tagging working point, corresponding to a b jet identification efficiency of approximately 70% for a light flavour and gluon jet misidentification rate of 1%. In case more than four jets are preselected, corresponding to less than 7% of the total signal events, the four highest p_T candidates are selected. The efficiency of the jet preselection on the SM HH signal is of about 7%.

The four preselected jets are combined into the two Higgs boson candidates H_1 and H_2. Correct jet pairing is determined as the combination that minimises the difference in the invariant mass of the two jet pairs. This allows to explore the signature of two resonant H → $b\bar{b}$ decays while minimising the bias induced in the multijet background selection, in particular suppressing jet combinations with both invariant masses close to m_H.

The signal region is defined by events that satisfy the following selection in the invariant mass

of the two Higgs boson candidates:

$$\sqrt{(\mathrm{m_{H_1}} - 120\,\mathrm{GeV})^2 + (\mathrm{m_{H_2}} - 120\,\mathrm{GeV})^2} < 40\,\mathrm{GeV} \quad (1)$$

The selection has an efficiency of about 55% on the HH signal and rejects approximately 85% of the QCD multijet background. The low selection efficiency for signal events is due to the removal of events where at least one of the selected jets does not originate from the decay of a Higgs boson, and cases where jets have been incorrectly paired. For events correctly reconstructed the selection efficiency corresponds to about 90%. The expected event yields after the invariant mass selections are approximately 1370 for the HH signal and 1.1×10^7 for the background, mostly consisting of QCD multijet and $\mathrm{t\bar{t}}$ events. This difference of almost four orders of magnitude between the two processes calls for the use of multivariate methods that exploit the kinematic differences between the HH signal and the background processes.

A multivariate discriminant, consisting of a boosted decision tree (BDT), is built using the following kinematic variables:

- the invariant mass of the two Higgs candidates $\mathrm{H_1}$ and $\mathrm{H_2}$
- the transverse momentum of the two Higgs candidates $\mathrm{H_1}$ and $\mathrm{H_2}$
- the four-jet invariant mass m_{HH}, and the reduced mass $M_{\mathrm{HH}} = m_{\mathrm{HH}} - (m_{\mathrm{H_1}} - 125\,\mathrm{GeV}) - (m_{\mathrm{H_2}} - 125\,\mathrm{GeV})$, the latter helping to remove part of the jet resolution effects by using the information on the Higgs boson invariant mass
- the minimal and max $\Delta\eta$ and $\Delta\varphi$ separation of the combinations of the four preselected jets
- the $\Delta\eta$, $\Delta\varphi$ and $\Delta\mathrm{R} = \sqrt{(\Delta\eta)^2 + (\Delta\varphi)^2}$ separation of the jets that constitute $\mathrm{H_1}$ and $\mathrm{H_2}$
- the cosine of the angle formed by one of the Higgs candidates with respect to the beam line axis in the HH system rest frame

The BDT is trained with a gradient boosting algorithm and its parameters are optimised to ensure the best performance while verifying that no overtraining is introduced. The output of the BDT is used as the discriminant variable to look for the presence of a signal as an excess at high output values. The expected distribution of signal and background events is illustrated in Fig. 1. The binning of the distribution is optimised to maximise the sensitivity to the SM HH signal.

In addition to the systematic uncertainties described in Section 3.3, uncertainties in the BDT shape are studied. We expect that the huge dataset collected at the HL-LHC will allow to make a precise estimate of the multijet background in signal-depleted regions, defined for example by the inversion of the b tag or invariant mass criteria. We thus consider an uncertainty of 5% on the BDT bins with the highest S/B ratio. A quantitative study of the impact of the size of such uncertainty is presented at the end of this section.

4.2 Event selection for boosted topologies

The regions of phase space having large m_{HH} are best explored using dedicated physics object reconstruction and event selections aimed at identifying highly Lorentz-boosted Higgs bosons, improving substantially the efficiency and performance for m_{HH} values larger than about 1 TeV. The bbbb final state is experimentally favorable in this context given its large branching fraction. As boosted object reconstruction methods in this final state have been already successfully applied to HH searches [39], this projection aims at investigating their potential at HL-LHC.

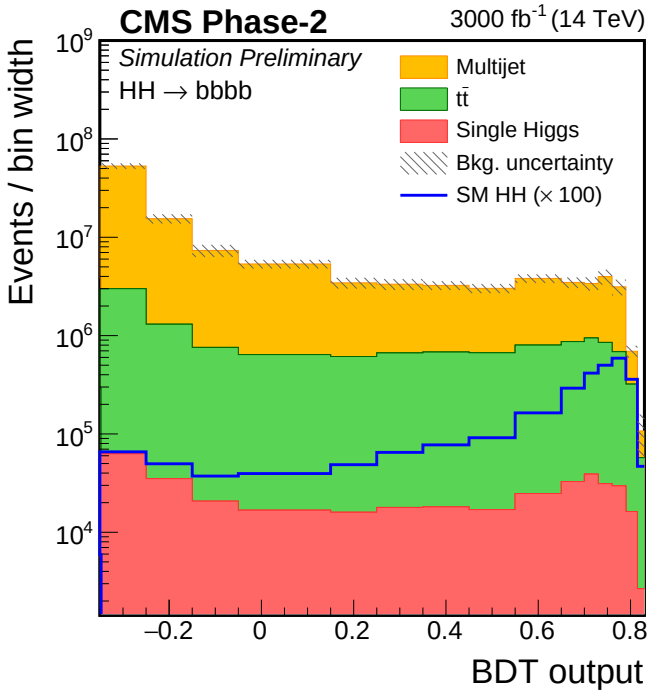

Figure 1: BDT output distribution for the signal and background processes considered in the bbbb resolved search.

Highly Lorentz-boosted H → $b\bar{b}$ decays are experimentally reconstructed as a single, large area jet. The particle-flow candidates are clustered using the anti-k_T algorithm with a distance parameter of 0.8 (AK8 jets). Contributions from pileup are mitigated using the pileup-per-particle (PUPPI) identification algorithm [40]. The vector sum of the clustered particle-flow candidates, weighted by their PUPPI weights, is assigned as the jet four-momentum. The jet energy is corrected to compensate for the nonlinear detector response to the energy deposited [41, 42].

The event selection aims to identify two boosted H → $b\bar{b}$ decays, each associated with a single AK8 jet. The two leading-p_T AK8 jets in the event, denoted as J_1 and J_2, are required to have $p_T > 300$ GeV and lie within $|\eta| < 3.0$. The soft-drop [43, 44] jet grooming algorithm is used to remove soft and collinear components of the jet and retain the two subjets associated with the showering and hadronization of the two b quarks from the H → $b\bar{b}$ decay. The jets J_1 and J_2 are both required to have a soft-drop mass between 90–140 GeV, consistent with the observed mass of 125 GeV for the Higgs boson.

To further reduce backgrounds, the N-subjettiness algorithm [45] is used, which can differentiate between a jet containing an N pronged decay from a jet containing a single hard parton. For a boosted H → $b\bar{b}$ jet with a two-pronged structure, the N-subjettiness ratio $\tau_{21} \equiv \tau_2/\tau_1$ is much smaller than unity, while the background jets have larger values. Consequently, a requirement of $\tau_{21} < 0.6$ is made for both J_1 and J_2. Both the soft-drop and the τ_{21} requirements are optimized using $S/\sqrt{B}$ as figure of merit.

The soft-drop subjets are b-tagged using the DeepCSV algorithm [46] which uses machine learning techniques with inputs based on the tracks and displaced vertices associated to the jets. In this search the jet b tagging probability for light flavoured jets is required to be about 1%, corresponding to a probability of about 49% to correctly identify jets containing a b hadron. Events are classified as those having exactly three (3b category) or exactly four (4b category)

b-tagged subjets, out of the four subjets belonging to J_1 and J_2.

The full event selection results in an efficiency for the SM signal of about 0.1%. For signals with a considerably harder m_{HH} spectrum, such as those represented by the shape benchmark number 2 used here as a reference, the selection efficiency is 1.8%.

The main background is dijet production in QCD interactions. In the analysis of true collision data, it is expected that the background will be obtained from the data itself. Here, simulated samples of QCD dijet events are used. The background estimation follows closely the approach in Ref. [47]. The background obtained from simulations is scaled by a factor of 0.7, which has been derived comparing the LHC data at $\sqrt{s} = 13\,\text{TeV}$ selected as described in [47], and a MC simulation for the 13 TeV conditions based on the same generator used in this work.

After the event selection, the expected number of SM HH signal events is 96 in the 3b and 15 in the 4b event categories. The most sensitive shape benchmark using the boosted event selection is benchmark 2, that is typically associated with strong contact interactions and hence characterised by a large fraction of events at high m_{HH}. For this signal, the events yields are 537 in the 3b and 61 in the 4b event categories, assuming a cross section of 10 fb. The corresponding background yields are 1.08×10^6 and 1.40×10^5 in the 3b and 4b categories, respectively.

The main discriminating variable between the signal and the background is the invariant mass of J_1 and J_2 m_{JJ}, which is correlated with the HH invariant mass. Figure 2 shows the m_{JJ} distributions of the signal and the background in the 3b and 4b event categories.

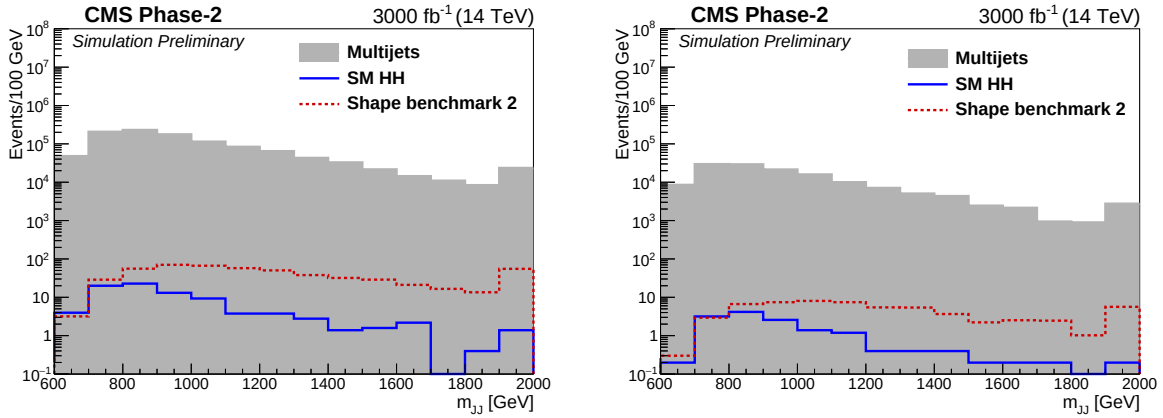

Figure 2: m_{JJ} distributions for the estimated multijet background and the SM (blue) and shape benchmark 2 (red) signals. The distributions on the left are for the 3b and those on the right are for the 4b subjet b-tagged categories. Both signals are normalised to the SM HH production cross section for visualisation.

In addition to the uncertainties described in Section 3.3, dedicated uncertainties to the objects and variables used in this analysis are considered. The H jet mass scale and resolution uncertainties correspond to 1% each, the uncertainty in the selection efficiency correction on τ_{21} amounts to 13%, and another 3.5% uncertainty is assigned to the modelling of the parton shower and hadronization of the $H \to b\bar{b}$ decay within the H jets. These uncertainties are taken from [48] and reduced by a factor of 1/2.

4.3 Results

The resolved analysis is used in the search for the SM HH signal and for the study of the anomalous λ_{HHH} couplings, while results on the expected constraint on anomalous HH production

in the context of EFT models are derived for the boosted search.

Using the resolved bbbb search strategy, upper limits are computed at 95% CL given the projected signal and background distributions shown in Fig. 1. Considering the systematic uncertainties discussed above, an upper limit of 2.1 times the SM prediction is expected, corresponding to a local significance of the expected HH signal of 0.95σ. If only statistical uncertainties are taken into account, the expected upper limit is 1.6 times the SM prediction and the significance is 1.2σ.

Challenges towards achieving these sensitivities at the HL-LHC will be the capability to develop efficient triggers for the bbbb signal, and to precisely model the multijet background.

Triggering on multi jet signatures will be particularly challenging at the HL-LHC and, despite the upgrades at the L1 trigger and HLT systems, thresholds might be significantly higher than currently achieved in Run II collisions. A study of the change in the search sensitivity as a function of the minimal jet p_{T} threshold is reported in Fig. 3. The study is realised by increasing the jet p_{T} value applied at preselection and studying the resulting changes in the sensitivity with respect to the nominal p_{T} threshold of 45 GeV discussed above. It has been verified that the loss of sensitivity does not arise from a reduced discrimination power of the BDT discriminant because of changes in the kinematic properties induced by the higher thresholds. Instead, the reduced sensitivity is a direct consequence of the reduced acceptance to HH → bbbb events, and an efficient trigger with low p_{T} thresholds will be crucial at the HL-LHC.

Changes in the SM HH significance as a function of the uncertainty on the high S/B bins for the QCD multijet background are also shown in Fig. 3.

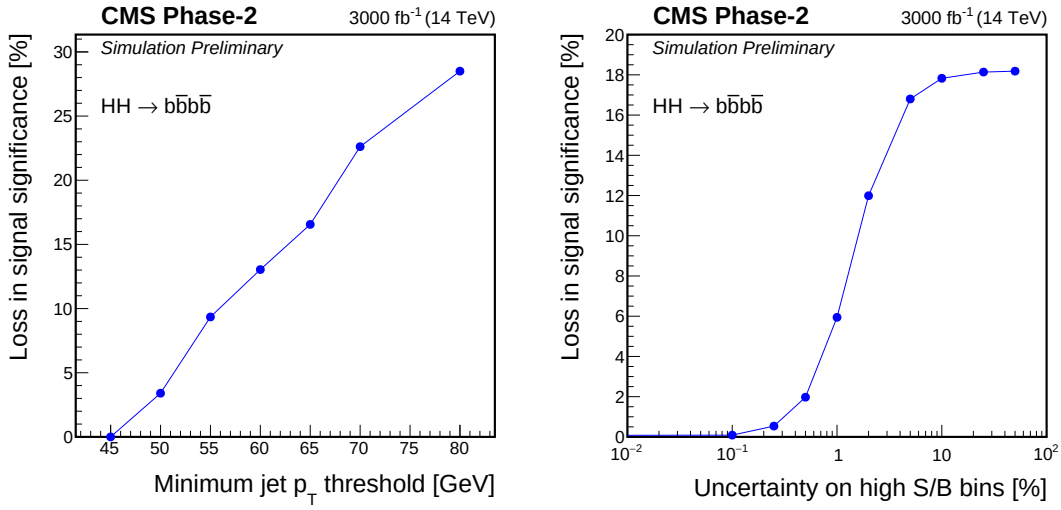

Figure 3: Loss of sensitivity of the HH → bbbb resolved search as a function of the minimal jet p_{T} threshold (left) and as a function of the uncertainty assumed on high S/B bins for the QCD multijet background (right). In each curve, only the quantity shown on the horizontal axis is varied while the other are kept fixed to the nominal values assumed. The "loss" quantity plotted on the ordinate is defined $1 - Z/Z^0$, where Z denotes the significance of the HH signal in the hypothesis considered and Z^0 the significance for the cases of a 45 GeV p_{T} threshold (left) and of no uncertainty considered (right).

Using the event yields and distributions shown in Fig. 2 for the boosted search strategy, we calculate the 95% confidence level (CL) upper limits on the nonresonant HH productions in the SM and for other combinations of BSM couplings using the shape benchmark signals 1–12, as

shown in Fig. 4.

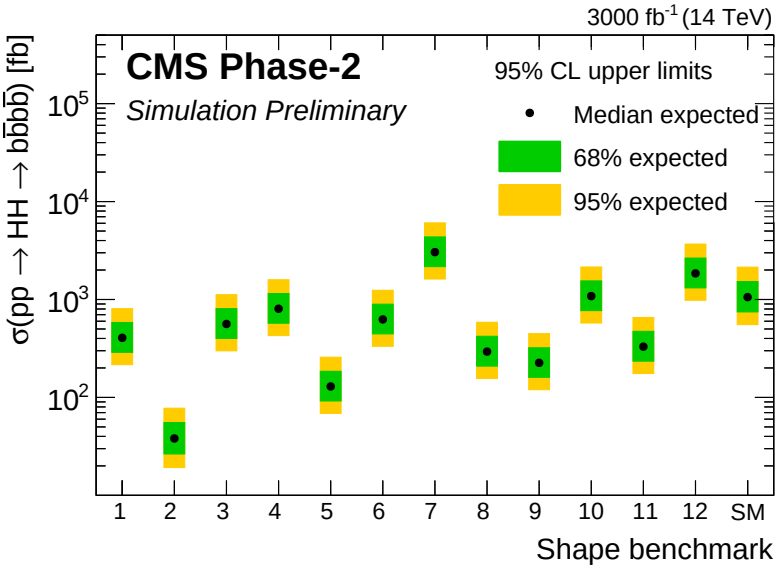

Figure 4: The expected upper limits for non-resonant HH production in the standard model and other shape benchmarks (1–12). The inner (green) and the outer (yellow) bands indicate the regions containing the 68 and 95%, respectively, of the distribution of limits expected under the background-only hypothesis.

5 $\mathrm{HH} \to \mathrm{bb}\tau\tau$

The $\mathrm{bb}\tau\tau$ final state is experimentally favourable thanks to its sizeable branching fraction of 7.3% and the moderate background contamination, mostly from irreducible processes such as $\mathrm{t\bar{t}} \to \mathrm{b\bar{b}W^+W^-}$ in a final state including a tau lepton and $\mathrm{Z}\gamma^* + \mathrm{b\bar{b}} \to \tau^+\tau^- + \mathrm{b\bar{b}}$, as well as instrumental backgrounds where jets are misidentified as hadronically decaying taus, τ_h. Furthermore, the presence of neutrinos in the final states represents a challenge to the signal identification as the final state is only partly reconstructed. State-of-the-art machine learning techniques are investigated here to study the search for a $\mathrm{HH} \to \mathrm{bb}\tau\tau$ signal at the HL-LHC.

5.1 Event selection

We assume that events will be collected by using single-lepton, lepton-plus-τ_h, and double-τ_h triggers with isolation criteria and transverse momentum thresholds similar to those used in Run II collisions. The assumptions appear reasonable considering the improved capabilities of the upgraded trigger system, the usage of track information in the L1 trigger to improve the τ_h reconstruction, and the possibility to develop more sophisticated kinematic triggers to specifically target the $\mathrm{HH} \to \mathrm{bb}\tau\tau$ signal. This work assumes the trigger efficiency to be 100% for the reconstructed object selections detailed below.

Decays of the $\tau\tau$ system can result in six final states: $\mathrm{e}\tau_\mathrm{h}$, $\mu\tau_\mathrm{h}$, $\tau_\mathrm{h}\tau_\mathrm{h}$, $\mu\mu$, $\mathrm{e}\mu$, and ee. In this study, we only consider the three final states involving at least one τ_h, that correspond to about 88% of the total decays of the $\tau\tau$ system and provide the largest sensitivity to the HH process.

Following the lepton and τ_h requirements defined in Tab. 2, events are exclusively selected into the three final state categories according to the following requirements:

Table 2: Kinematic requirements (p_T, η, and isolation) of electrons, muons, and hadronic taus. The hadronic tau requirements are listed according to the final states considered.

Lepton	Min. p_T [GeV]	Max. $\lvert\eta\rvert$	Max. iso [GeV]
Primary μ	23	2.1	0.15
Primary e	27	2.1	0.1
Veto e/μ	10	2.4	0.3
Hadronic tau	**Min. p_T [GeV]**	**Max. $\lvert\eta\rvert$**	
$\ell\tau_h$bb ($\ell = e, \mu$)	20	2.3	
$\tau_h\tau_h$bb	45	2.1	

- $\mu\tau_h$: exactly one primary muon with no additional muons or electrons that satisfy looser veto selections, and at least one τ_h of opposite charge to the primary muon;
- eτ_h: exactly one primary electron with no additional muons or electrons that satisfy looser veto selections, and at least one τ_h of opposite charge to the primary electron;
- $\tau_h\tau_h$: exactly zero veto muons or electrons and at least two τ_h of opposite charge to one another. In case of multiple possible choices of τ_h candidate, the highest p_T ones are selected.

Events in all the three categories above are also required to contain at least two b-tagged jets with $p_T > 30\,\text{GeV}$, $|\eta| < 2.4$. After these selections, about 100, 70 and 60 SM HH signal events are expected in the $\mu\tau_h$, eτ_h, and $\tau_h\tau_h$ decay channels respectively. The corresponding total number of background events for the three channels are, respectively, 4.3×10^6, 2.9×10^6, and 1.25×10^3, mostly dominated by $t\bar{t}$ and Drell-Yan $\tau\tau$ production.

The selected visible $\tau\tau$ decay products, the b jets, and the missing transverse momentum are used to build the two Higgs boson candidates. The $H_{\tau\tau}$ candidate is defined as the sum of the four momenta of the selected lepton and τ_h in the $\mu\tau_h$ and eτ_h final states, and as the sum of the two τ_h four momenta in the $\tau_h\tau_h$ final state, plus the vector of missing momentum projected onto the plane transverse to the beam axis. Similarly, the $H_{b\bar{b}}$ candidate is defined as the sum of the four momenta of the two selected b jets. Finally, the four momentum of the HH system is computed as the vector sum of the selected object four momenta plus the vector of missing momentum projected onto the plane transverse to the beam axis.

5.2 DNN discriminant

5.2.1 Input variables to the neural network discriminant

Kinematic properties of the selected events in each of the three bb$\tau\tau$ final states are used to develop a neural network discriminant that is capable of separating the signal contribution from the background processes. A total of 52 input variables, also denoted as features, are used in this study. They are split into *basic* (27), *high-level/reconstructed* (21), and *high-level/global* (4) features. The specific choice of the input variables, as described below, was chosen since these proved to give the best discriminator performance, while other features could be implicitly computed by the network.

In what follows, τ_0 is defined as the τ_h in $\ell\tau_h$bb events and as the highest p_T τ_h candidate in $\tau_h\tau_h$bb events, while τ_1 is defined as the other selected lepton or τ_h. Additionally, we label the highest p_T b jet as b_0 and the other as b_1.

5.2.1.1 Basic features 27 low-level final state features are calculated during the event reconstruction process: the 4-momenta in Cartesian coordinates (i.e. $\left(p_x, p_y, p_z, E\right)$), the magnitude of the 3-momenta, and mass of each selected final state (τ_0, τ_1, b_0, and b_1); and the magnitude of missing transverse momentum ($p_{\mathrm{T}}^{\mathrm{miss}}$), and its transverse components (p_x^{miss} and p_y^{miss}).

5.2.1.2 High level reconstructed features 21 reconstructed features are calculated:

- The 4-momenta, magnitude of 3-momenta, and the invariant masses of the three systems which correspond to:
  1. the Higgs boson that decays to $\mathrm{b\bar{b}}$ ($\mathrm{H_{b\bar{b}}}$),
  2. the Higgs boson that decays to $\tau\tau$ ($\mathrm{H}_{\tau\tau}$), and
  3. the di-Higgs-boson system (HH);
- the stransverse mass (M_{T2}) of the system [49, 50];
- the transverse masses (m_T) of each tau, calculated according to Eq. 2:

$$m_T = \sqrt{2p_{T,\tau} \times p_{\mathrm{T}}^{\mathrm{miss}} \times \left(1 - \cos\Delta\phi_{\tau, p_{\mathrm{T}}^{\mathrm{miss}}}\right)}. \tag{2}$$

5.2.1.3 High level global features Four features help characterise the global event by returning the overall kinematics of physics objects and the (tagged) jet multiplicities:

- s_T, the scalar sum of muon p_{T}, tau p_{T}, b jet p_{T}, and $p_{\mathrm{T}}^{\mathrm{miss}}$;
- the total number of jets (inclusive), b jets, and τ jets.

Example distributions of some of the features are shown in Fig. 5.

5.2.2 Architecture and training summary

The dataset of simulated signal and background events, selected as described in the previous section, is divided into two equally sized subsamples and a pair of discriminators is trained, one on each half of the data. In Sec. 5.3, each discriminator is then used to classify the events in the subsample on which it was not trained.

Each discriminant consists of an ensemble of ten fully-connected deep neural networks (DNN), each consisting of three hidden layers of 100 neurons with SELU [51] activation functions. They are implemented in KERAS [52] using TENSORFLOW [53] as a back-end. The training and inference procedures make use of the improvements described in Ref. [54], however all improvements were reverified in this context using the approximate median significance (AMS), as defined in Ref. [55], as the optimisation metric. The various improvements were found to increase on the AMS by about 30% compared to the original model.

5.3 Signal inference

5.3.1 Summary statistic construction

The expected discovery significances and cross section upper limits at 95% confidence are determined by considering the output of the DNN as a summary statistic of the signal and background events, and performing the hypothesis test of signal+background versus the null hypothesis of background-only in multiple regions of the statistic, spanning its full range (a shape analysis). This is achieved by parametrising the density of the signal and background events

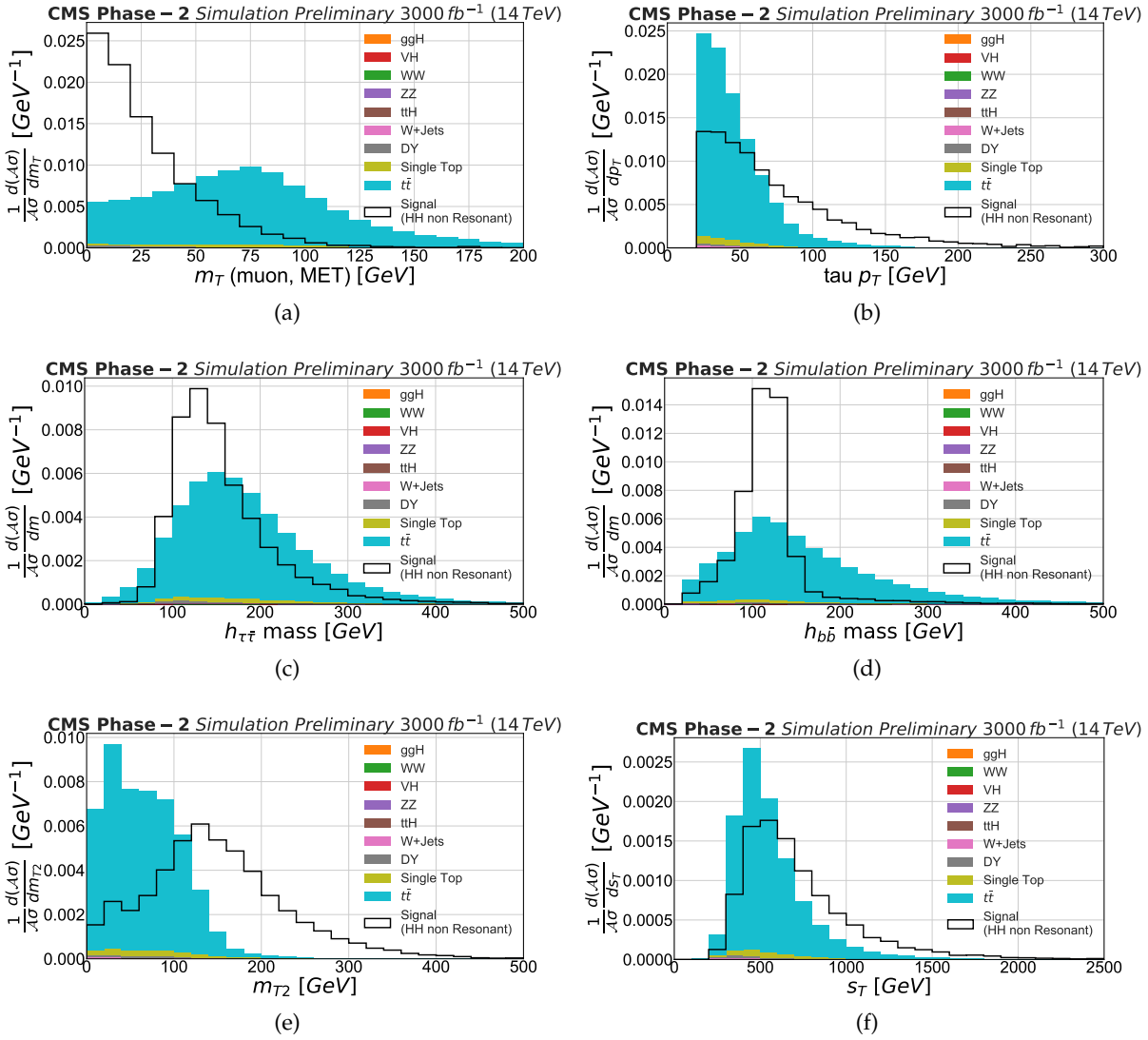

Figure 5: Example distributions for some of the features of the signal and background processes. Low-level features in the $\mu\tau_h$ final-state:
(a) Transverse mass of the muon (i.e. τ_μ), as defined in Eq. 2,
(b) Transverse momentum of the τ_h.
Higgs-candidate masses for all final states together:
(c) $H_{\tau\tau}$ mass,
(d) $H_{b\bar{b}}$ mass.
High-level features for all final-states channels together:
(e) The stransverse mass M_{T2},
(f) s_T (defined as the scalar sum of lepton p_T, p_T of both b-jets and τ_h, and p_T^{miss}).
Distributions are normalized to unit areas for signal and background, separately.

using histograms of variable bin width in order to better capture the shape of the distributions whilst not causing the statistical uncertainties in each bin to become too large. This process is done on a per decay-channel basis, resulting in three sets of distributions.

In order to make better use of the MC samples available, two DNN ensembles are trained, each on half of the samples. Each half of the data is then classified by the ensemble that was not trained on it. Since we make no fine-tuning of network hyper-parameters, and the architecture development was performed over cross-validation, each half of the data that was not used for training an ensemble represents an unseen sample of data for that ensemble. In doing this, we are able to classify the entire of our MC samples without the performance being biased due to overfitting.

Signal and background events are binned such that in a given bin, the statistical uncertainty on the population of each signal and background sample is less than 30%. However, only background samples with at least 100 MC events and a yield greater than 50 times that of the signal are considered when defining the bin edges, ensuring that the background samples considered have a sufficient number of simulated events to populate the distributions. These requirements aim to prevent our expected performance from being unduly limited by the sizes of the Monte Carlo samples currently available.

5.3.2 Hypothesis testing and results

A simultaneous fit is performed on the expected event distributions for the three final states considered, considering the systematic uncertainties described in Section 3.3. The uncertainty due to the number of MC events falling in each bin are neglected under the assumption that samples of sufficient size will be available for HL-LHC analyses.

With the assumed systematic uncertainties, an upper limit on the HH cross section times branching fraction of 1.4 times the SM prediction is obtained, corresponding to a significance of 1.4σ. If only statistical uncertainties are considered, the upper limit amounts to 1.3 times the SM prediction for a significance of 1.6σ.

6 $HH \rightarrow bbWW$

We consider here HH final states containing two b jets and two neutrinos and two leptons, either electrons or muons. The decay channels involved are thus $H \rightarrow b\bar{b}$ in association with either a $H \rightarrow Z(\ell\ell)Z(\nu\nu)$ or a $H \rightarrow W(\ell\nu)W(\ell\nu)$ decay. While the analysis described in the following is optimised for $HH \rightarrow bbWW$ decays, that provide the largest branching fraction, the contribution of Higgs boson decays to both WW and ZZ, globally denoted as VV, is considered. Decays of the VV system to tau leptons subsequently decaying to electrons or muons with the associated neutrinos are also considered in the simulated signal samples. The corresponding branching fraction for the $VV \rightarrow \ell\nu\ell\nu$ decay is 1.73 % [19].

The dominant and subdominant background processes are $t\bar{t}$ production in its fully leptonic decay mode, and Drell-Yan production of lepton pairs in association with jets. As both are irreducible background processes, i.e. they result in the same final state as the signal, the kinematic properties of the signal and background events are used and combined in an artificial Neural Network (NN) discriminant to enhance the sensitivity.

The single Higgs boson production backgrounds $t\bar{t}H$ and $H \rightarrow WW(\ell\nu\ell\nu)$ were also considered but were found to have a negligible effect on the final result.

6.1 Event selection and background predictions

Events are selected based on the same selection criteria currently applied in the Run II CMS analysis of this final state. We assume that such events will be selected with dilepton triggers with transverse momentum thresholds similar to those deployed in Run II collisions, providing a 100% efficiency for the events that satisfy the selection described below.

Events are required to contain two leptons of opposite electric charge (e^+e^-, $\mu^+\mu^-$, $e^\pm\mu^\mp$), and with p_T greater than 25 GeV and 15 GeV for ee events, 20 GeV and 10 GeV for $\mu\mu$ events, 25 GeV and 15 GeV for μe events, 25 GeV and 10 GeV for eμ events, for the higher and lower p_T lepton, respectively. Electrons and muons in the pseudo-rapidity range $|\eta| < 2.8$ are considered, except the $1.444 < |\eta| < 1.5666$ being rejected for electrons. A dilepton mass requirement of $m_{\ell\ell} > 12$ GeV is applied to all flavour combinations in order to suppress leptonia resonances.

Jets are required to have $p_T > 20$ GeV, $|\eta| < 2.8$, and be separated from identified leptons by a distance of $\Delta R = \sqrt{\Delta\phi^2 + \Delta\eta^2} > 0.3$. The magnitude of the negative vector sum of all PF candidates is referred to as p_T^{miss}. Selected jets must also satisfy the medium working point of the b tagging algorithm.

A summary of the object definitions and selections is shown in Table 3.

Table 3: Object definitions and event selections requirements.

Object	ID and isolation requirements	Selection
Electrons	Isolation ($\|\eta\| > 1.5666$) > 0.559 (0.853)	$\|\eta\| < 1.444$ or $1.5666 < \|\eta\| < 2.8$ Leading $p_T > 25$ GeV Sub-leading $p_T > 20$ GeV
Muons	Loose ID, Isolation < 0.25	$\|\eta\| < 2.8$ Leading $p_T > 20$ GeV in $\mu\mu$ events Leading $p_T > 25$ GeV in μe events Sub-leading $p_T > 10$ GeV in $\mu\mu$ and eμ events
Jets	PUPPI Jet	$p_T > 20$ GeV, $\|\eta\| < 2.4$, $\Delta R_{lj} > 0.3$
B-Jets	PUPPI medium MTD WP	$p_T > 20$ GeV, $\|\eta\| < 2.8$

Among all possible di-jets combinations fulfilling the previous criteria we select the two jets with the highest combined transverse momentum.

After the final object selection consisting of two opposite sign leptons and two b-tagged jets, a cut on $m_Z - m_{\ell\ell} > 15$ GeV is applied to remove the resonant Z peak and the high-$m_{\ell\ell}$ tail of the Drell-Yan+jets and $t\bar{t}$ background process.

The performance of the selections and object reconstruction was extensively checked looking at different kinematic distributions and comparing them to the ones obtained in the analysis of CMS data collected in the Run II.

After all the selection requirements described in this section, a total of about 50, 150, and 120 SM HH signal events is expected in the ee, eμ, and $\mu\mu$ decay channels, respectively. The total numbers of background events in the three categories are 2.9×10^6, 8.4×10^6, and 7.5×10^6, respectively. The dominant background is $t\bar{t}$ production, with a sizeable contribution from Drell-Yan lepton pair production in the same-flavour dilepton channels.

6.2 Signal extraction

A neural network (NN) discriminant, based on the TMVA software [56], is used to improve the signal-to-background separation. In a phase space dominated by $\mathrm{t\bar{t}}$ production, the NN utilizes information related to object kinematics. The variables provided as input to the NN exploit the presence of two Higgs bosons decaying into two b-jets on the one hand, and two leptons and two neutrinos on the other hand, which results in different kinematics for the di-lepton and di-jet systems between signal and background processes. The set of variables used as input is: $m_{\ell\ell}$, m_{jj}, $\Delta R_{\ell\ell}$, ΔR_{jj}, $\Delta\phi_{\ell\ell,jj}$, defined as the $\Delta\phi$ between the di-jet and the di-lepton systems, $p_T^{\ell\ell}$, p_T^{jj}, $\min(\Delta R_{j,\ell})$, and M_T, defined as $M_T = \sqrt{2p_T^{\ell\ell} p_T^{miss}(1-\cos(\Delta\phi(\ell\ell, p_T^{miss})))}$.

The output of the NN after selections in the e^+e^-, $\mu^+\mu^-$, $e^\pm\mu^\mp$ channels, is shown in Fig. 6. The Drell-Yan production of lepton pairs is modelled by interpolating separately in the three channels the simulated selected events with a third degree polynomial function, used to generate a smooth event distribution according to the expect event yields. The smoothing procedure has little impact on the projected sensitivity as discussed below.

As no shape uncertainty is considered in the $\mathrm{t\bar{t}}$ background modelling and the total number of events for small NN output values is expected to reach tens of millions, the search may be subject to over-constraints of any systematic uncertainty that may be dependent or correlated with the $\mathrm{t\bar{t}}$ shape. In order to mitigate this effect, the signal-depleted region with a NN output smaller than 0.5 will be excluded from the statistical inference.

6.3 Results

The results are derived as upper limits on the HH signal strength, defined as the ratio of the signal cross section times branching fraction to the SM expectation. A simultaneous fit is performed on the distributions of events shown in Fig. 6 in the e^+e^-, $\mu^+\mu^-$ and $e^\pm\mu^\mp$ event categories.

The expected upper limit at the 95% CL corresponds to 3.5 times the SM prediction when systematic uncertainties are considered, and to 3.3 times the same value if only statistical uncertainties are assumed. The corresponding significance of the HH signal is 0.56 and 0.59σ, respectively.

The impact of the assumed Drell-Yan contribution was shown to be small by scaling its expected yield by factors of 0.5 and 2 and verifying the changes in the sensitivity. Variations of 5% or below in the final result were observed, showing that the result is robust under different assumptions on the Drell-Yan background contamination.

7 $\mathrm{HH} \to \mathrm{bb}\gamma\gamma$

While characterized by a tiny branching fraction, the $\mathrm{bb}\gamma\gamma$ final state is experimentally very clean and thus provides a large sensitivity. The main background processes are the continuum production of diphoton events and of single photons in association with a misidentified jet, as well as single Higgs boson production, where the Higgs boson decays to $\gamma\gamma$.

7.1 Selection

We assume that events selected as described below will be triggered with algorithms that require the presence of two photons and that are 100% efficient for selected events. This assumption is well verified in the current Run II search.

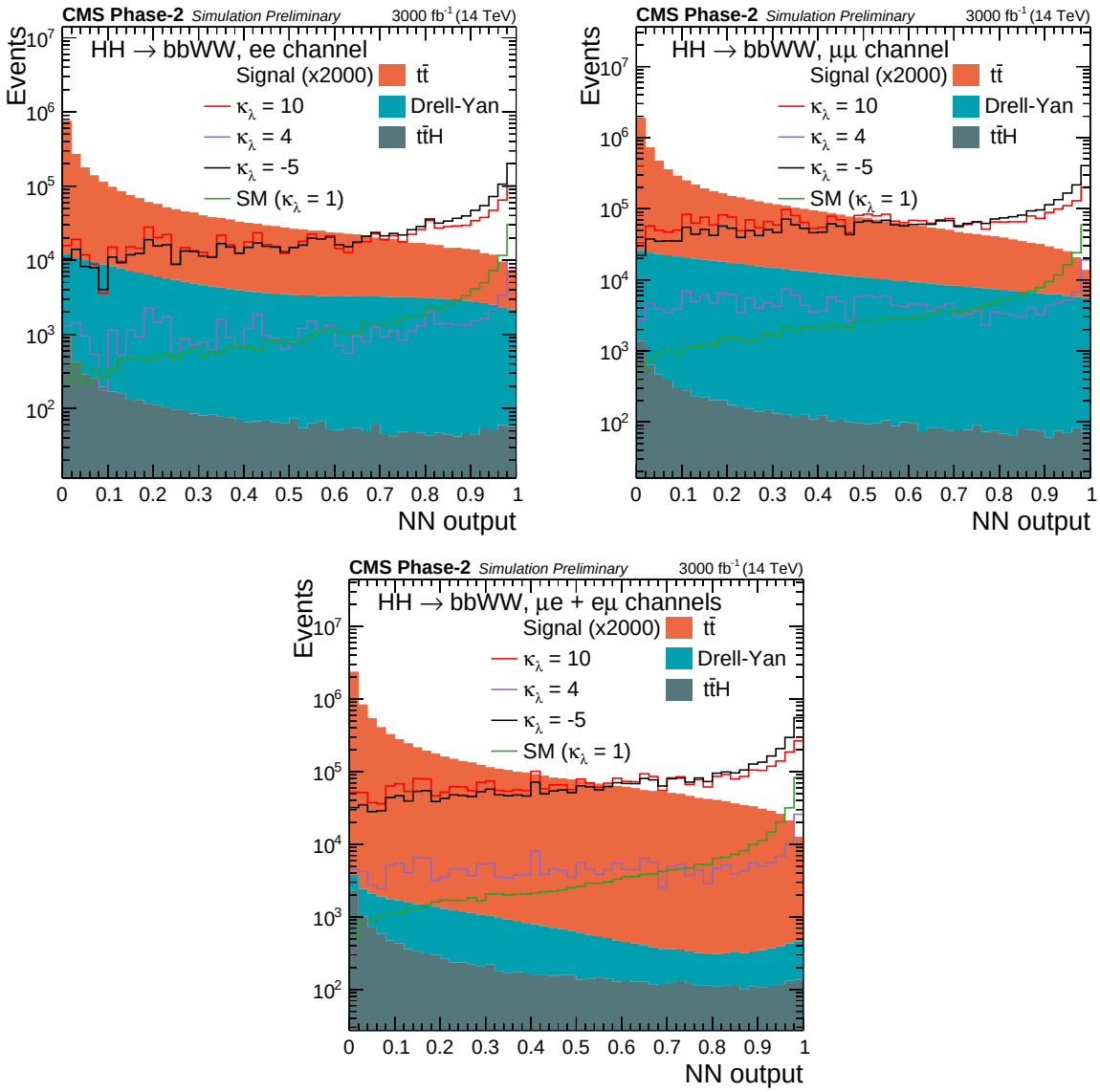

Figure 6: The output of the NN after the selections, evaluated in the e^+e^- (top left) , $\mu^+\mu^-$ (top right), $e^\pm\mu^\mp$ (bottom) channels.

Photons satisfying the loose working point, corresponding to an efficiency of about 90% for a photon with $p_T > 30\,GeV$ and a jet misidentification rate of about 3%, are selected. The two photons with the highest p_T that satisfy such requirements are considered and used to build the $H \to \gamma\gamma$ candidate, and the kinematic selections reported in Table 4 are applied. While the acceptance of photons in the upgraded detector extends up to $\eta = 3$, the pseudorapidity is limited to 2.5 in order to increase the signal to background ratio. For events selected in the most sensitive categories, as described below, the signal photons are more central than background ones. An additional selection in η is applied to exclude the transition region from the barrel electromagnetic to the endcap calorimeters.

The $H \to b\bar{b}$ candidate is built from jets that satisfy the kinematic selection reported in Table 4. As discussed above, the $|\eta| < 2.5$ requirement is applied in order to increase the signal to background ratio. The angular distance $\Delta R_{\gamma j}$ between the jets and the selected photons is required to be larger than 0.4. In case more than two jets satisfy the kinematic requirements described

above, candidates satisfying the highest b tagging criteria are preferred. In case ambiguities in the choice persist, the higher p_T objects are selected. The background from light flavour jets is suppressed by requiring both jets to satisfy the loose working point of the b tagging algorithm, corresponding roughly to a 90% efficiency for a genuine b-jet and 10% of fake rate from jets initiated by light quarks or gluons. In addition, the dijet invariant mass m_{jj} is required to be between 80 and 190 GeV.

Table 4: Photon and jet kinematic selections.

Photon selections
$p_T/m_{\gamma\gamma} > 1/3$ (leading γ), $> 1/4$ (subleading γ)
$\lvert\eta\rvert < 1.44$ or $1.57 < \lvert\eta\rvert < 2.5$
$100\,\text{GeV} < m_{\gamma\gamma} < 180\,\text{GeV}$
Jet selections
$p_T > 25\,\text{GeV}$
$\lvert\eta\rvert < 2.5$
$\Delta R_{\gamma j} > 0.4$
$80\,\text{GeV} < m_{jj} < 190\,\text{GeV}$
At least 2 b-tagged jet (loose WP)

The invariant mass of the $\gamma\gamma jj$ system is denoted as $m_{\gamma\gamma jj}$. The jet and photon resolution effects in $m_{\gamma\gamma jj}$ are mitigated by defining the variable M_X as:

$$M_X = m_{\gamma\gamma jj} - m_{\gamma\gamma} - m_{jj} + 250\ \text{GeV} \tag{3}$$

After such kinematic preselections, the main background contribution comes from nonresonant diphoton events. The main resonant backgrounds consist of Higgs boson production in association with two top quarks ($t\bar{t}H$), as expected because of their topology that is very similar to the signal. This background source is suppressed with the usage of a dedicated multivariate discriminant, consisting of a BDT trained to separate the HH and $t\bar{t}H$ processes. The discriminant combines twelve variables related to the presence of additional jets, electrons or muons, as well as the helicity angles of the HH and $b\bar{b}$ systems. A selection is applied on the output of the discriminant, rejecting approximately 75% of the $t\bar{t}H$ contamination for a signal efficiency of 90%. The selection on the BDT output was optimized based on the expected significance for the SM HH signal hypothesis.

7.2 Event categorization

A categorization based on a multivariate discriminant is performed. A BDT is trained to discriminate the signal from the sum of background processes. The $t\bar{t}H$ process is not considered because of the dedicated $t\bar{t}H$ discriminant described above. The variables used for the BDT training are:

- minimum angular distance between the selected jets and the selected photons. This variable is expected to reject collinear photon emission from a quark characteristic of QCD processes.
- angle between the diphoton object and the beam axis in the $\gamma\gamma jj$ rest-frame.
- angle between the leading selected jet and the beam axis in the dijet rest-frame.

- angle between the leading selected photon and the beam axis in the diphoton rest-frame.
- ratio of the transverse momentum to the mass, p_T/M, for the selected diphotons and dijets.
- b tag output for the two selected jets.
- photon energy resolution σ_E/E for the two selected photons.
- angles on transverse plane between the direction of the missing momentum and the two selected jets.
- numbers of loose, medium, tight b-tagged jets in the event

It has been verified that the selection applied on the BDT output does not sculpt the diphoton and dijet invariant mass distributions for background events. Events with a low BDT classifier output are rejected, allowing to suppress approximately 90% of the background events including QCD events with light quarks. The events thus selected are divided in a medium and a high purity category based on the BDT output. The high purity (HP) category provides the best sensitivity and collects approximately 35% of the preselected events, while the medium purity (MP) category increases the overall acceptance to about 75% of the signal events, contributing to the overall sensitivity. Events are further divided into three categories depending on their M_X value. For each category an optimization on the separation between MP and HP is performed to maximize the sensitivity to the SM HH production, and the SM HH signal is approximately equally shared among the resulting categories. The event categorization is summarized in Table 5.

In total, considering all the categories and a region centred on the $m_{\gamma\gamma}$ signal peak with a width of 2 times its resolution, about 40 SM HH signal events are expected to be recorded, for a total of about 190 resonant background events and 3600 nonresonant background events, approximately. High mass categories provide the best sensitivity to the SM HH signal, with about 35 signal events expected and a total of about 1600 background events. Low mass categories are sensitive to variations of the Higgs boson self coupling, that may enhance the production cross section at low m_{HH} values.

Table 5: Categorisation applied for events selected in the $bb\gamma\gamma$ analysis. The symbols MP and HP denote, respectively, the medium and high purity categories based on the BDT output.

MVA category	Classification on M_X
0: HP 1: MP	$250 < M_X < 350$ GeV:
2: HP 3: MP	$350 < M_X < 380$ GeV
4: HP 5: MP	$480 < M_X$ GeV

7.3 Results

The background distributions are modelled by fitting the selected MC event distribution with an exponentially falling distribution, that was observed to describe well the simulated events. Results are obtained with a simultaneous fit of a pseudodataset (Asimov dataset) constructed from the modelled signal and background distributions in the categories defined above. An illustration of the expected distributions of events in the three high purity categories for the

photon and jet pairs invariant mass is shown in Fig. 7. The events are obtained by generating random distribution with a Poissonian statistics from the Asimov dataset including SM signal and background.

The expected 95% CL upper limits on the HH signal is 1.09 times the HH cross section when systematic uncertainties are considered, and 1.11 when only statistical uncertainties are accounted for. The corresponding significance of the HH signal is 1.83 and 1.85σ, respectively.

8 HH $\rightarrow$ bbZZ

Up to now, the low signal rate leads to consider mostly final states with a sizable branching ratio. In view of HL-LHC, some rare but clean processes have been re-considered because of the increasing available statistics and the challenging conditions due to the enormous number of pile-up events. In this work, the sensitivity to the Higgs self-coupling for m_H = 125 GeV is evaluated through the measurement of the non-resonant di-Higgs production final states in the bbZZ (4ℓ) decay mode, where $\ell = e, \mu$. Despite a small cross section ($\sigma_{b\bar{b}4\ell} = 5.3\,ab$), the presence of four leptons associated with two b jets leads to a very clean final state topology allowing to maintain a rather good signal selection efficiency and to control the backgrounds. The main background processes are $t\bar{t}H(ZZ)$, $t\bar{t}Z$, ggH and ZH, followed by minor contributions such as WH and single Higgs production via vector boson fusion (VBF). The $t\bar{t}ZZ$ and $t\bar{t}H(WW)$ contributions are found to be negligible. Top quark pair production and Drell-Yan (DY) lepton pair production in association to jets are a reducible background for the analysis. As their contamination is due to hadrons misidentified as leptons (fake leptons) or to the selection of non-prompt leptons, large suppressions are expected with the selections used in this work. Nevertheless, their huge cross section, orders of magnitude larger than the HH signal, makes them a challenging background at the HL-LHC. The estimation of the $t\bar{t}$ and DY contribution in this work is difficult because of the limited number of MC events available, leading to very large uncertainties related to the few or zero events satisfying the selections. Moreover, the actual impact of the $t\bar{t}$ and DY backgrounds on the analysis largely depends on reconstruction techniques and performance in the rejection of fake and non-prompt leptons that are not fully optimized in the parametric simulation implemented in Delphes. We assume that dedicated techniques and optimized algorithms will be available by the HL-LHC operations to have negligible contamination, deeming this assumption reasonable from studies performed on the MC simulation. We also remark that the size of MC samples will not represent an issue at the HL-LHC, given the possibility to control the effective contaminations in data control regions. Nevertheless, the developments of such methods will represent a major challenge towards HL-LHC to maintains a high sensitivity in the bbZZ(4ℓ) channel. Signal and background samples are simulated as described in Section 3. In addition to the SM scenario ($\kappa_\lambda = 1$), samples with several other values of κ_λ, ranging from $\kappa_\lambda = -10$ to $\kappa_\lambda = 10$, are generated.

8.1 Event Selection

Events are required to have at least four identified and isolated (isolation < 0.7) muons (electrons) with $p_T > 5(7)$ GeV and $|\eta| < 2.8$, where muons (electrons) are selected if passing the loose (medium) working point identification. Z boson candidates are formed from pairs of opposite-charge, same flavour leptons ($\ell^+\ell^-$) requiring a minimum angular separation between two leptons of 0.02. At least two di-lepton pairs are required. The Z candidate with the invariant mass closest to the nominal Z mass is denoted as Z_1; then, among the other opposite-sign lepton pairs, the one with the highest p_T is labelled as Z_2. In order to improve the sensitivity to the Higgs boson decay, Z candidates are required to have an invariant mass in the range

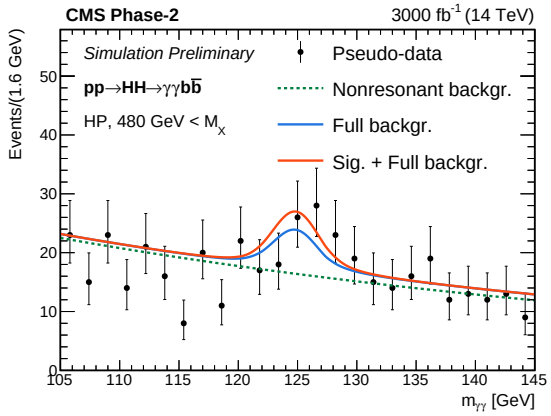

(a) $m_{\gamma\gamma}$, high mass category

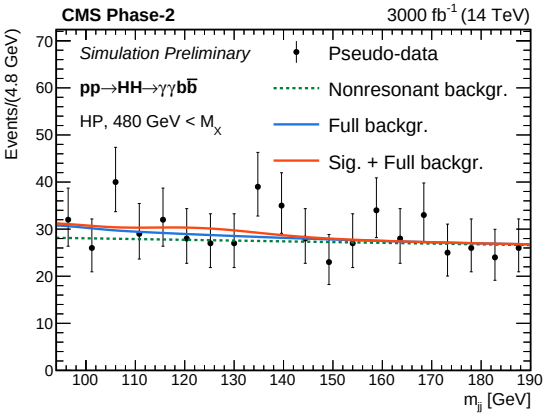

(b) m_{jj}, high mass category

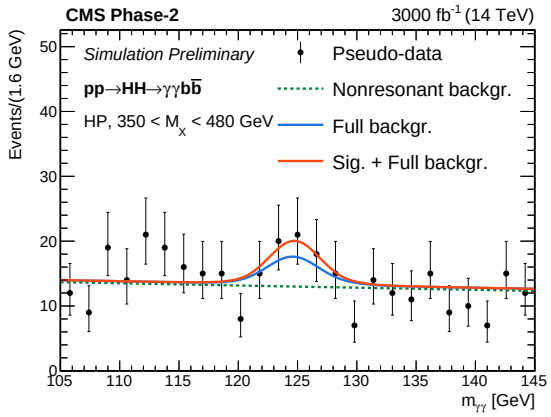

(c) $m_{\gamma\gamma}$, medium mass category

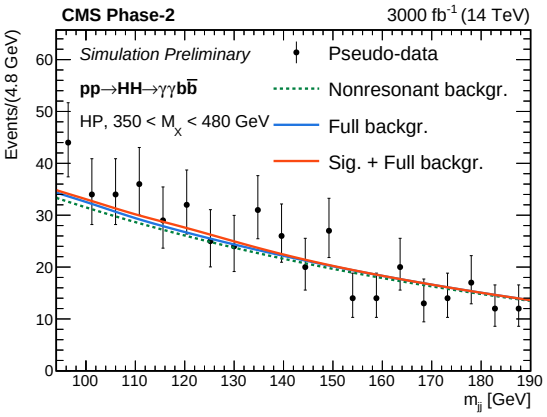

(d) m_{jj}, medium mass category

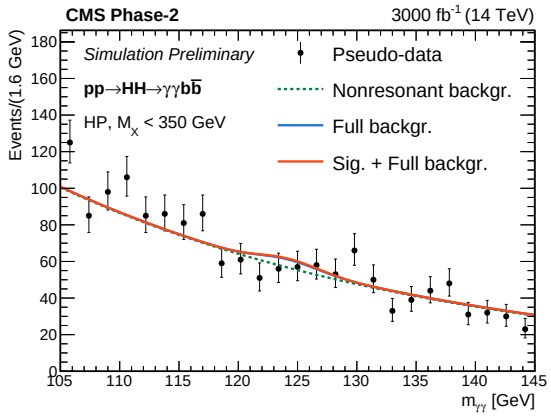

(e) $m_{\gamma\gamma}$, low mass category

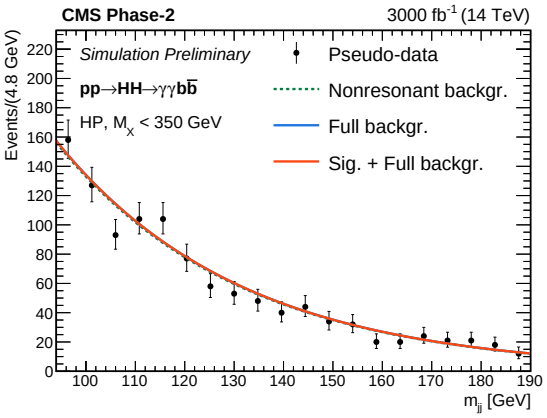

(f) m_{jj}, low mass category

Figure 7: Expected distribution of events in the photon (left column) and jet (right column) pair invariant mass. The full circles denote pseudo-data obtained from the expected events yields for the sum of the signal and background processes for 3000 fb^{-1}. Only the most sensitive high purity category is shown.

[50, 100] GeV (Z_1) and [12, 60] GeV (Z_2), respectively. At least one lepton is required to have $p_T > 20$ GeV and a second is required to have $p_T > 10$ GeV. The four leptons invariant mass, $m_{4\ell}$, is requested to be in the range [120, 130] GeV.

At least two (but not more than three) identified b jets, reconstructed with the anti-k_T algorithm inside a cone of radius $R = 0.4$, are required; a b tag Medium working point is assumed. Their invariant mass, corrected assuming an improvement of 20% on the resolution on the $m_{b\bar{b}}$ peak, as expected for HL-LHC thanks to a proper b jet energy regression, is required to be in the range [90, 150] GeV. The angular distance between the two b jets has to be $0.5 < \Delta R_{b\bar{b}} < 2.3$; furthermore, the missing transverse energy of the event must be smaller than 150 GeV, and a selection on the angular distance between the two reconstructed Higgs is set to $\Delta R_{HH} \geq 2.0$.

8.2 Results

The invariant mass spectrum of the four leptons after the full event selection is shown in Figure 8. Considering the channels investigated, we expect to select 1 HH event for a total background yield of 6.8 in the inclusive $b\bar{b}4\ell$ (ℓ = e, μ) final state.

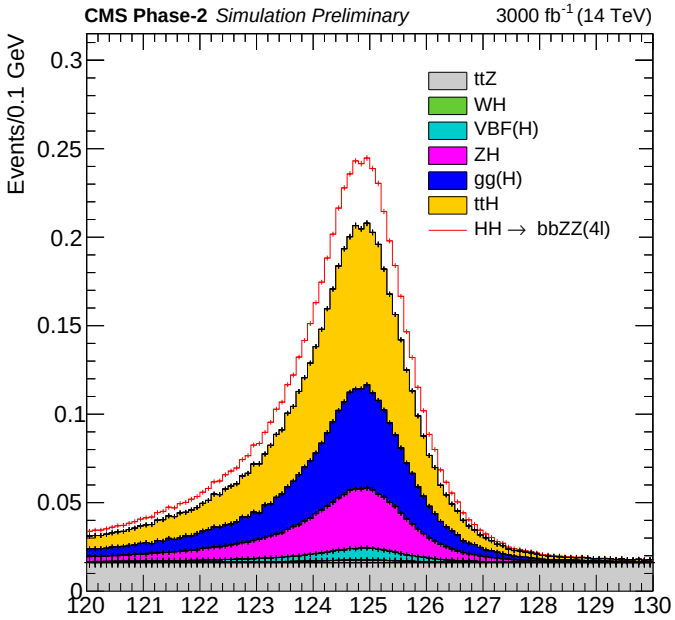

Figure 8: Invariant mass distribution of the four leptons selected at the end of the analysis for the $b\bar{b}4\ell$ final state.

The combined upper limit at the 95% CL on the HH cross section corresponds to 6.6 times the SM prediction, with a corresponding significance of 0.37σ. The impact of the systematic uncertainties on the analysis is found to be almost negligible. The most sensitive channel is $b\bar{b}4\mu$, but a sizeable contribution to the sensitivity also comes from the $b\bar{b}2e2\mu$ and $b\bar{b}4e$ final states.

9 Decay channel combination and results

The results obtained in the five decay channels described above are combined statistically assuming the SM branching fractions for HH decays to the final states studied. The analyses

of the five decay channels are designed to be orthogonal thanks to the mutually exclusive requirements in the objects used, or to have negligible overlap due to tight object identification criteria and the separation and the efficient separation achieved by the multivariate methods used. Systematic uncertainties associated to the same objects, such as the b tag efficiency uncertainties, and to the same processes, including common backgrounds and the HH signal, are correlated across the corresponding decay channels, while the others are left uncorrelated.

Table 6 summarises, for the five channels and their combination, the upper limit at the 95% confidence level (CL) and the significance for the SM HH signal. The combined 95% CL upper limit on the SM HH cross section amounts to 0.77 times the SM prediction, with a corresponding significance of the signal of 2.6σ. These results significantly improve over previous projections thanks to the dedicated optimisation of the analysis strategies to the HL-LHC dataset. In comparison, the extrapolation to an integrated luminosity of $3000\,\text{fb}^{-1}$ of the current Run II combination, obtained with a dataset of $35.9\,\text{fb}^{-1}$ collected at $\sqrt{s} = 13\,\text{TeV}$ [57], yields a projected SM HH significance of 1.8σ neglecting all the systematic uncertainties.

Table 6: Upper limit at the 95% confidence level, significance, projected measurement at 68% confidence level of the Higgs boson self coupling λ_{HHH} for the five channels studied and their combination. Systematic and statistical uncertainties are considered.

Channel	Significance		95% CL limit on $\sigma_{\text{HH}}/\sigma_{\text{HH}}^{\text{SM}}$	
	Stat. + syst.	Stat. only	Stat. + syst.	Stat. only
bbbb	0.95	1.2	2.1	1.6
bb$\tau\tau$	1.4	1.6	1.4	1.3
bbWW($\ell\nu\ell\nu$)	0.56	0.59	3.5	3.3
bb$\gamma\gamma$	1.8	1.8	1.1	1.1
bbZZ($\ell\ell\ell\ell$)	0.37	0.37	6.6	6.5
Combination	2.6	2.8	0.77	0.71

Prospects for the measurement of the λ_{HHH} coupling are also studied. Under the assumption that no HH signal exists, 95% CL upper limits on the SM HH production cross section are derived as a function $\kappa_\lambda = \lambda_{\text{HHH}}/\lambda_{\text{HHH}}^{\text{SM}}$, where $\lambda_{\text{HHH}}^{\text{SM}}$ denotes the SM prediction. The result is illustrated in Fig. 9. A variation of the excluded cross section, directly related to changes in the HH kinematic properties, can be observed as a function of λ_{HHH}. In the case of the bbWW analysis, these changes largely impact the DNN discriminant distribution that is optimised for the SM point. Parametrisation techniques, similar to those deployed in the Run II search, and further optimisations can be envisaged at the HL-LHC to mitigate this effect and improve the constraint on λ_{HHH}.

Assuming instead that a HH signal exists with the properties predicted by the SM, prospects for the measurement of the λ_{HHH} are derived. The scan of the likelihood as a function of the κ_λ coupling is shown in Fig. 10. The projected confidence interval on this coupling corresponds to $[0.35, 1.9]$ at the 68% CL and to $[-0.18, 3.6]$ at the 95% CL. The peculiar likelihood function structure, characterised by two local minimums, is related to the dependence of the total cross section and HH kinematic properties on κ_λ, while the relative height of the two minimums depends to the capability of the analyses to access differential m_{HH} information. The total HH cross section has a quadratic dependence on κ_λ with a minimum at $\kappa_\lambda \approx 2.45$, while the kinematic differences for signals with κ_λ values symmetric around this minimum are mostly relevant in the low region of the m_{HH} spectrum. Consequently, a partial degeneracy exists between the $\kappa_\lambda = 1$ value, that is assumed for the expected signal plus background modelling

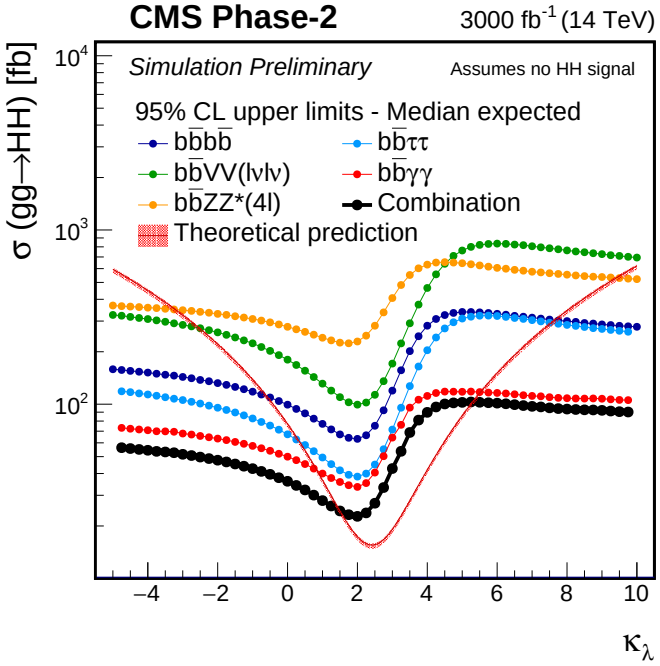

Figure 9: Upper limit at the 95% CL on the HH production cross section as a function of $\kappa_\lambda = \lambda_{\mathrm{HHH}}/\lambda^{\mathrm{SM}}_{\mathrm{HHH}}$ for the five decays channels investigated and their combination. The red band indicated the theoretical production cross section.

in the results of Fig 10, and a second κ_λ value. The exact position of this second minimum depends on the interplay between the changes in the cross section and in the acceptance as a function of κ_λ. In analyses that retain sensitivity on the differential m_{HH} distribution, such as bbbb and bb$\tau\tau$ where this information is used as input to the multivariate methods, this degeneracy is partly removed. In the case of the bb$\gamma\gamma$ analysis, with a good acceptance and purity in the low m_{HH} region and a dedicated m_{HH} categorisation, a better discrimination of the second minimum is achieved. Further improvements can be envisaged in HL-LHC analyses by extending the m_{HH} categorisation to other channels beyond bb$\gamma\gamma$.

The combination of the five channels largely removes the degeneracy, and results in a plateau in the likelihood function for κ_λ values between 4 and 6. Improvements in the combined sensitivity in this region have a large effect on the size of the 95% CL interval for the κ_λ measurement.

10 Summary

Prospects for the search of Higgs boson pair (HH) production and for the measurement of the Higgs boson self-coupling (λ_{HHH}) at the High-Luminosity LHC (HL-LHC) are presented. The study is performed using the five decay channels of the HH system to bbbb, bb$\tau\tau$, bbWW (with both W decaying leptonically), bb$\gamma\gamma$, and bbZZ (with both Z decaying to a pair of electrons or muons). The response of the upgraded CMS detector is studied with a parametric simulation that accounts for an average of 200 pp interactions per bunch crossing, and simulates the performance in the reconstruction and identification of physics objects. Assuming that no HH signal exists, a 95% confidence level (CL) upper limit on its cross section can be set to 0.77 times the SM prediction. Assuming that a HH signal exists with the properties predicted by the SM, we expect a combined significance of 2.6σ and a determination of the λ_{HHH} coupling corresponding to the interval $[0.35, 1.9]$ at the 68% CL and to $[-0.18, 3.6]$ at the 95% CL.

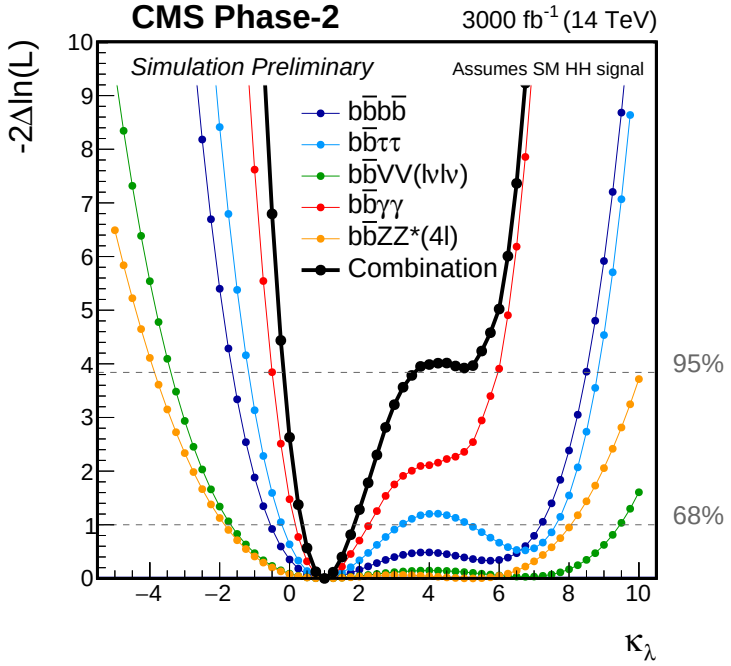

Figure 10: Expected likelihood scan as a function of $\kappa_\lambda = \lambda_{\mathrm{HHH}}/\lambda^{\mathrm{SM}}_{\mathrm{HHH}}$. The functions are shown separately for the five decay channels studied and for their combination.

References

[1] ATLAS Collaboration, "Observation of a new particle in the search for the Standard Model Higgs boson with the ATLAS detector at the LHC", *Phys. Lett. B* **716** (2012) 1, doi:10.1016/j.physletb.2012.08.020, arXiv:1207.7214.

[2] CMS Collaboration, "Observation of a new boson at a mass of 125 GeV with the CMS experiment at the LHC", *Phys. Lett. B* **716** (2012) 30, doi:10.1016/j.physletb.2012.08.021, arXiv:1207.7235.

[3] CMS Collaboration, "Observation of a new boson with mass near 125 GeV in pp collisions at $\sqrt{s}$ = 7 and 8 TeV", *JHEP* **06** (2013) 081, doi:10.1007/JHEP06(2013)081, arXiv:1303.4571.

[4] ATLAS and CMS Collaborations, "Measurements of the Higgs boson production and decay rates and constraints on its couplings from a combined ATLAS and CMS analysis of the LHC pp collision data at $\sqrt{s} = 7$ and 8 TeV", *JHEP* **08** (2016) 045, doi:10.1007/JHEP08(2016)045, arXiv:1606.02266.

[5] F. Englert and R. Brout, "Broken symmetry and the mass of gauge vector mesons", *Phys. Rev. Lett.* **13** (1964) 321, doi:10.1103/PhysRevLett.13.321.

[6] P. W. Higgs, "Broken symmetries and the masses of gauge bosons", *Phys. Rev. Lett.* **13** (1964) 508, doi:10.1103/PhysRevLett.13.508.

[7] G. S. Guralnik, C. R. Hagen, and T. W. B. Kibble, "Global conservation laws and massless particles", *Phys. Rev. Lett.* **13** (1964) 585, doi:10.1103/PhysRevLett.13.585.

[8] F. Goertz, A. Papaefstathiou, L. L. Yang, and J. Zurita, "Higgs boson pair production in the D=6 extension of the SM", *JHEP* **04** (2015) 167, doi:10.1007/JHEP04(2015)167, arXiv:1410.3471.

[9] M. Grazzini et al., "Higgs boson pair production at NNLO with top quark mass effects", *JHEP* **05** (2018) 059, doi:10.1007/JHEP05(2018)059, arXiv:1803.02463.

[10] ATLAS Collaboration, "Studies of the ATLAS potential for Higgs self-coupling measurements at a High Luminosity LHC", Technical Report ATL-PHYS-PUB-2013-001, CERN, Geneva, 2013.

[11] ATLAS Collaboration, "Higgs Pair Production in the $H(\to \tau\tau)H(\to b\bar{b})$ channel at the High-Luminosity LHC", Technical Report ATL-PHYS-PUB-2015-046, CERN, Geneva, 2015.

[12] ATLAS Collaboration, "Prospects for Observing $t\bar{t}HH$ Production with the ATLAS Experiment at the HL-LHC", Technical Report ATL-PHYS-PUB-2016-023, CERN, Geneva, 2016.

[13] ATLAS Collaboration, "Study of the double Higgs production channel $H(\to b\bar{b})H(\to \gamma\gamma)$ with the ATLAS experiment at the HL-LHC", Technical Report ATL-PHYS-PUB-2017-001, CERN, Geneva, 2017.

[14] CMS Collaboration, "Higgs pair production at the High Luminosity LHC", CMS Physics Analysis Summary CMS-PAS-FTR-15-002, CERN, Geneva, 2015.

[15] CMS Collaboration, "Projected performance of Higgs analyses at the HL-LHC for ECFA 2016", CMS Physics Analysis Summary CMS-PAS-FTR-16-002, CERN, Geneva, 2016.

[16] CMS Collaboration, "The Phase-2 Upgrade of the CMS Tracker", Technical Report CERN-LHCC-2017-009. CMS-TDR-014, CERN, Geneva, 2017.

[17] CMS Collaboration, "The Phase-2 Upgrade of the CMS Barrel Calorimeters Technical Design Report", Technical Report CERN-LHCC-2017-011. CMS-TDR-015, CERN, Geneva, 2017.

[18] CMS Collaboration, "The Phase-2 Upgrade of the CMS Endcap Calorimeter", Technical Report CERN-LHCC-2017-023. CMS-TDR-019, CERN, Geneva, 2017.

[19] D. de Florian et al., "Handbook of LHC Higgs cross sections: 4. Deciphering the nature of the Higgs sector", CERN Report CERN-2017-002-M, 2016. doi:10.23731/CYRM-2017-002, arXiv:1610.07922.

[20] CMS Collaboration, "Technical Proposal for the Phase-II Upgrade of the CMS Detector", Technical Report CERN-LHCC-2015-010. LHCC-P-008. CMS-TDR-15-02, CERN, Geneva, 2015.

[21] CMS Collaboration, "Expected performance of the physics objects with the upgraded CMS detector at the HL-LHC", Technical Report CMS-NOTE-2018-006, CERN, Geneva, 2018.

[22] DELPHES 3 Collaboration, "DELPHES 3, A modular framework for fast simulation of a generic collider experiment", *JHEP* **02** (2014) 57, doi:doi:10.1007/JHEP02(2014)057, arXiv:1307.6346.

[23] J. Alwall et al., "The automated computation of tree-level and next-to-leading order differential cross sections, and their matching to parton shower simulations", *JHEP* **07** (2014) 079, doi:10.1007/JHEP07(2014)079, arXiv:1405.0301.

[24] A. Carvalho et al., "On the reinterpretation of non-resonant searches for Higgs boson pairs", arXiv:1710.08261.

[25] A. Carvalho et al., "Higgs Pair Production: Choosing Benchmarks With Cluster Analysis", *JHEP* **04** (2016) 126, doi:10.1007/JHEP04(2016)126, arXiv:1507.02245.

[26] P. Nason, "A New method for combining NLO QCD with shower Monte Carlo algorithms", *JHEP* **11** (2004) 040, doi:10.1088/1126-6708/2004/11/040, arXiv:hep-ph/0409146.

[27] S. Frixione, P. Nason, and C. Oleari, "Matching NLO QCD computations with Parton Shower simulations: the POWHEG method", *JHEP* **11** (2007) 070, doi:10.1088/1126-6708/2007/11/070, arXiv:0709.2092.

[28] S. Alioli, P. Nason, C. Oleari, and E. Re, "A general framework for implementing NLO calculations in shower Monte Carlo programs: the POWHEG BOX", *JHEP* **06** (2010) 043, doi:10.1007/JHEP06(2010)043, arXiv:1002.2581.

[29] S. Frixione, P. Nason, and G. Ridolfi, "A Positive-weight next-to-leading-order Monte Carlo for heavy flavour hadroproduction", *JHEP* **09** (2007) 126, doi:10.1088/1126-6708/2007/09/126, arXiv:0707.3088.

[30] T. Sjöstrand et al., "An Introduction to PYTHIA 8.2", *Comput. Phys. Commun.* **191** (2015) 159–177, doi:10.1016/j.cpc.2015.01.024, arXiv:1410.3012.

[31] M. Czakon and A. Mitov, "Top++: A Program for the Calculation of the Top-Pair Cross-Section at Hadron Colliders", *Comput. Phys. Commun.* **185** (2014) 2930, doi:10.1016/j.cpc.2014.06.021, arXiv:1112.5675.

[32] M. Aliev et al., "HATHOR: HAdronic Top and Heavy quarks crOss section calculatoR", *Comput. Phys. Commun.* **182** (2011) 1034–1046, doi:10.1016/j.cpc.2010.12.040, arXiv:1007.1327.

[33] P. Kant et al., "HatHor for single top-quark production: Updated predictions and uncertainty estimates for single top-quark production in hadronic collisions", *Comput. Phys. Commun.* **191** (2015) 74–89, doi:10.1016/j.cpc.2015.02.001, arXiv:1406.4403.

[34] S. Agostinelli et al., "Geant4-a simulation toolkit", *Nuclear Instruments and Methods in Physics Research Section A: Accelerators, Spectrometers, Detectors and Associated Equipment* **506** (2003), no. 3, 250 – 303, doi:https://doi.org/10.1016/S0168-9002(03)01368-8.

[35] M. Cacciari, G. P. Salam, and G. Soyez, "The anti-k_t jet clustering algorithm", *JHEP* **04** (2008) 063, doi:10.1088/1126-6708/2008/04/063, arXiv:0802.1189.

[36] M. Cacciari, G. P. Salam, and G. Soyez, "FastJet User Manual", *Eur. Phys. J.* **C72** (2012) 1896, doi:10.1140/epjc/s10052-012-1896-2, arXiv:1111.6097.

[37] D. Bertolini, P. Harris, M. Low, and N. Tran, "Pileup Per Particle Identification", *JHEP* **10** (2014) 059, doi:10.1007/JHEP10(2014)059, arXiv:1407.6013.

[38] CMS Collaboration, "Technical proposal for a MIP timing detector in the CMS experiment Phase 2 upgrade", Technical Report CERN-LHCC-2017-027. LHCC-P-009, CERN, 2017.

[39] CMS Collaboration, "Search for production of Higgs boson pairs in the four b quark final state using large-area jets in proton-proton collisions at $\sqrt{s} = 13$ TeV", arXiv:1808.01473.

[40] D. Bertolini, P. Harris, M. Low, and N. Tran, "Pileup Per Particle Identification", *JHEP* **10** (2014) 059, doi:10.1007/JHEP10(2014)059, arXiv:1407.6013.

[41] CMS Collaboration, "Jet energy scale and resolution in the CMS experiment in pp collisions at 8 TeV", *JINST* **12** (2017) P02014, doi:10.1088/1748-0221/12/02/P02014, arXiv:1607.03663.

[42] CMS Collaboration, "Jet energy scale and resolution performances with 13 TeV data", CMS Detector Performance Summary CMS-DP-2016-020, CERN, 2016.

[43] M. Dasgupta, A. Fregoso, S. Marzani, and G. P. Salam, "Towards an understanding of jet substructure", *JHEP* **09** (2013) 029, doi:10.1007/JHEP09(2013)029, arXiv:1307.0007.

[44] A. J. Larkoski, S. Marzani, G. Soyez, and J. Thaler, "Soft drop", *JHEP* **05** (2014) 146, doi:10.1007/JHEP05(2014)146, arXiv:1402.2657.

[45] J. Thaler and K. Van Tilburg, "Maximizing boosted top identification by minimizing N-subjettiness", *JHEP* **02** (2012) 093, doi:10.1007/JHEP02(2012)093, arXiv:1108.2701.

[46] CMS Collaboration, "Identification of heavy-flavour jets with the CMS detector in pp collisions at 13 TeV", *JINST* (2017) doi:10.1088/1748-0221/13/05/P05011, arXiv:1712.07158.

[47] CMS Collaboration, "Search for vector boson fusion production of a massive resonance decaying to a pair of Higgs bosons in the four b quark final state at the HL-LHC using the CMS Phase 2 detector", CMS Physics Analysis Summary CMS-PAS-FTR-18-003, CERN, Geneva, 2018.

[48] CMS Collaboration, "Search for a massive resonance decaying to a pair of Higgs bosons in the four b quark final state in proton-proton collisions at $\sqrt{s} = 13$ TeV", *Phys. Lett. B* **781** (2018) 244, doi:10.1016/j.physletb.2018.03.084, arXiv:1710.04960.

[49] M. M. Nojiri, Y. Shimizu, S. Okada, and K. Kawagoe, "Inclusive transverse mass analysis for squark and gluino mass determination", *JHEP* **06** (2008) 035, doi:10.1088/1126-6708/2008/06/035, arXiv:0802.2412.

[50] C. G. Lester and D. J. Summers, "Measuring masses of semiinvisibly decaying particles pair produced at hadron colliders", *Phys. Lett.* **B463** (1999) 99–103, doi:10.1016/S0370-2693(99)00945-4, arXiv:hep-ph/9906349.

[51] G. Klambauer, T. Unterthiner, A. Mayr, and S. Hochreiter, "Self-normalizing neural networks", *CoRR* **abs/1706.02515** (2017) arXiv:1706.02515.

[52] F. Chollet et al., "Keras". https://keras.io, 2015.

[53] M. Abadi et al., "TensorFlow: Large-scale machine learning on heterogeneous systems", 2015. Software available from tensorflow.org. http://tensorflow.org/.

[54] The AMVA4NewPhysics ITN, "Classification and regression tools in higgs measurements", *ITN Deliverable, Work Package 1* (2018). https://userswww.pd.infn.it/~dorigo/d1.4.pdf.

[55] G. Cowan, "Discovery sensitivity for a counting experiment with background uncertainty",. http://www.pp.rhul.ac.uk/~cowan/stat/medsig/medsigNote.pdf and also talk slides http://www.pp.rhul.ac.uk/~cowan/atlas/cowan_statforum_8may12.pdf.

[56] A. Hoecker et al., "TMVA: Toolkit for Multivariate Data Analysis", *PoS* **ACAT** (2007) 040, arXiv:physics/0703039.

[57] CMS Collaboration, "Combination of searches for Higgs boson pair production in proton-proton collisions at $\sqrt{s} = 13$ TeV", arXiv:1811.09689.